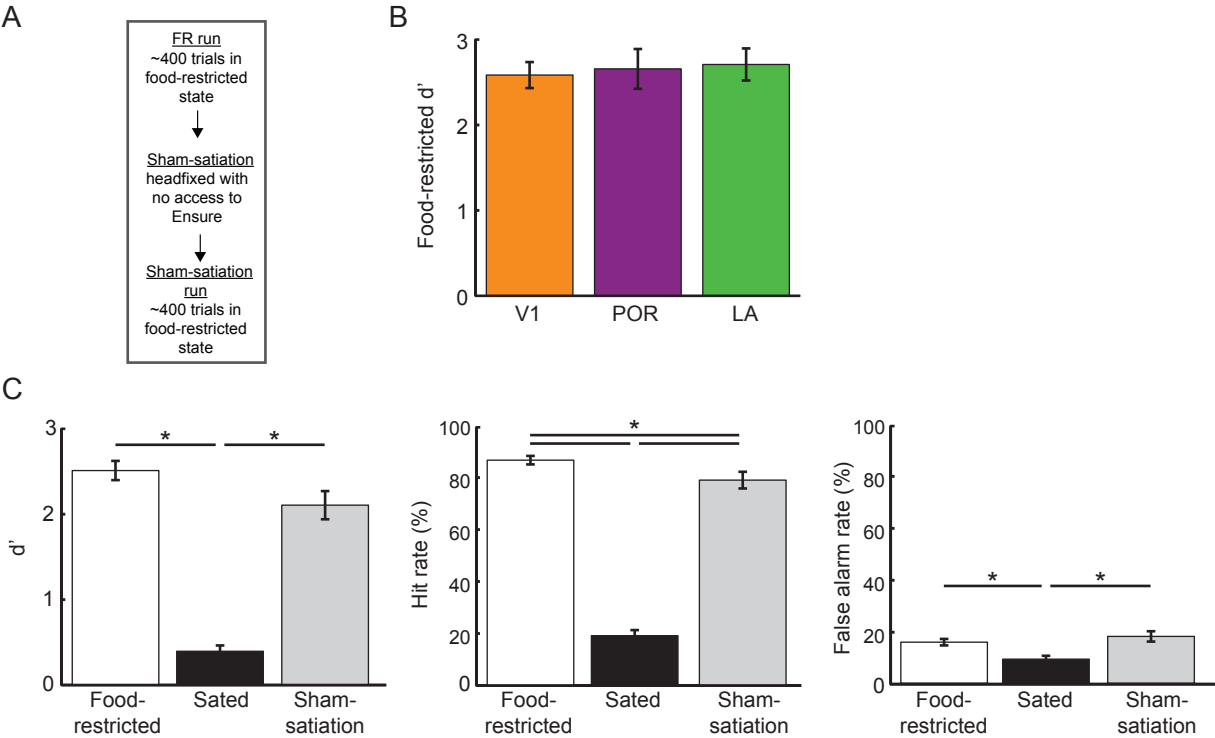


Figure S1



**Figure S1. Related to Figure 1. Mice accurately perform the visual discrimination task**

- A. As a control for time elapsed between blocks of trials during food-restricted and sated states, in other 'sham-satiation' sessions an equal duration of time elapsed between early and late sets of ~400 trials, but without delivery of Ensure.
- B. Task performance (discriminability,  $d'$ ) was not different across mice used for recordings from V1, POR, or  $LA^{\rightarrow POR}$  neurons. \*  $p < 0.05$  ANOVA; Errorbars, SEM.
- C. Mice performed the head-fixed visual discrimination task with high behavioral accuracy when food-restricted. Discriminability ( $d'$ ), hit rate and false alarm rate were all significantly decreased from the food-restricted (or from the sham-satiation) state to the sated state (see Supplemental Experimental Procedures).

Figure S2

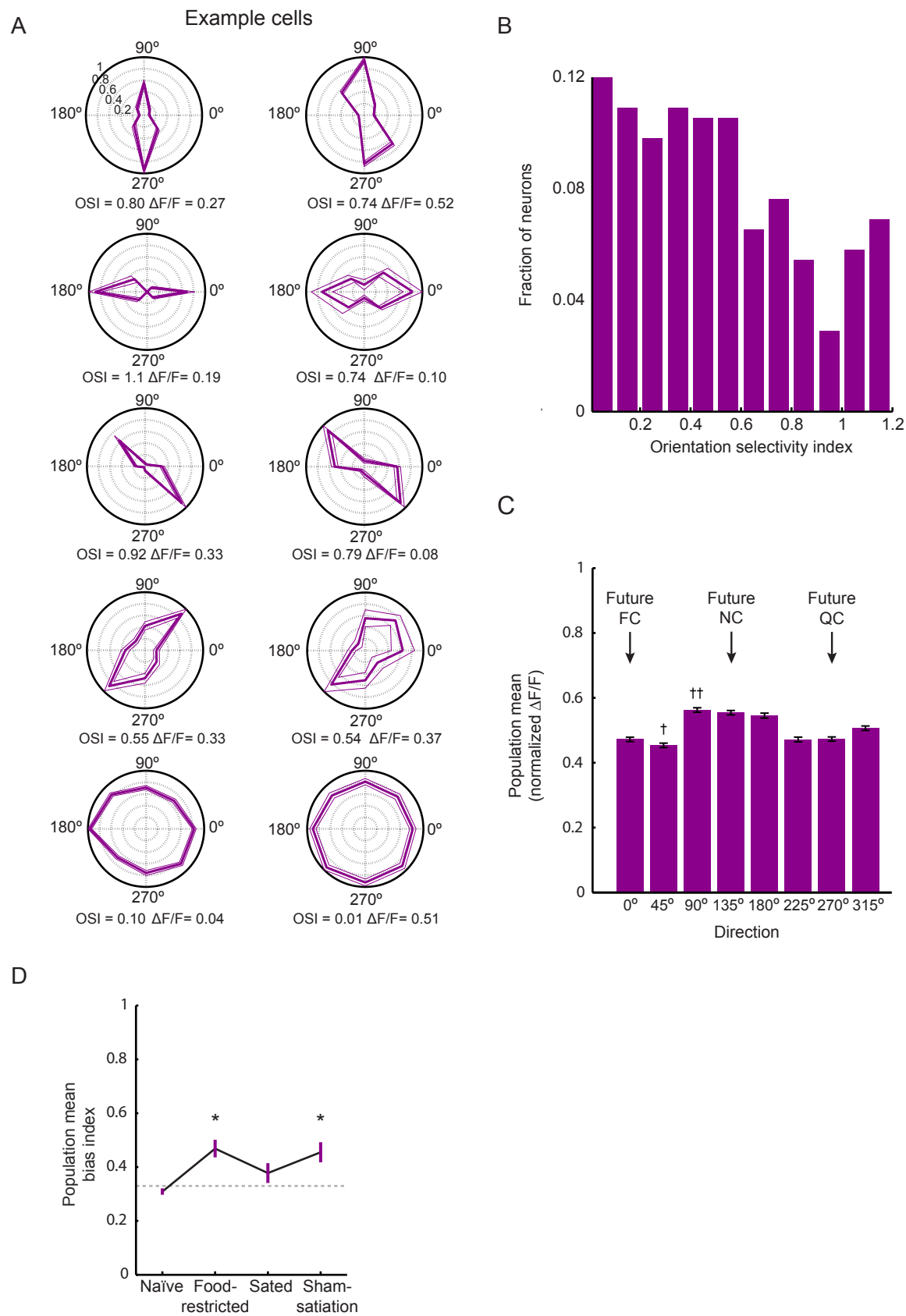


**Figure S2. Related to Figure 2. No response bias to the FC across POR neurons in naïve, untrained mice**

- A. Example direction tuning curves (in polar coordinates) from neurons in POR of a naïve, untrained mouse, generated using drifting square-wave gratings (see Supplemental Experimental Procedures; 90°: upward motion; 0°: rightward motion). Thick lines denote mean response, thin lines denote SEM. Orientation selectivity indices (OSIs, see Supplemental Experimental Procedures) and maximal response magnitudes ( $\Delta F/F$ ) are listed at lower right. Many POR neurons were strongly orientation tuned.
- B. Distribution of OSIs across all visually-responsive neurons (n=276) in POR. High OSI values indicate neurons with sharp orientation tuning, while low OSI values indicate broadly tuned neurons.
- C. In naïve, untrained mice (n=4), there was no significant difference in the average population response (average of peak-normalized tuning curves) in POR to any of the cues used in training, including the stimulus direction that we paired with Ensure availability (i.e. the FC). †  $p < 0.05$  45° vs. 90°, 135°, 180°. ††  $p < 0.05$  90° vs. 0°, 225°, 270°;  $p > 0.05$  for all other comparisons, Kruskal-Wallis). Errorbars, SEM.
- D. When sub-selecting only those cells that were visually responsive to at least one of the three directions used in the discrimination task (future FC, QC, NC) and calculating the FC bias index ( $[FC]/[FC+QC+NC]$ ), we did not observe a bias to the FC in naïve, untrained animals. Specifically, when compared with data from trained animals, we only observed a significant bias during food-restricted and sham-satiation conditions in trained mice, but not during sated states in either trained or naïve mice ( $p < 0.005$  food-restricted;  $p < 0.005$  sham-satiation;  $p > 0.05$  naïve/sated; Wilcoxon Sign-Rank test against 0.33 (chance), Bonferroni corrected).



Figure S3

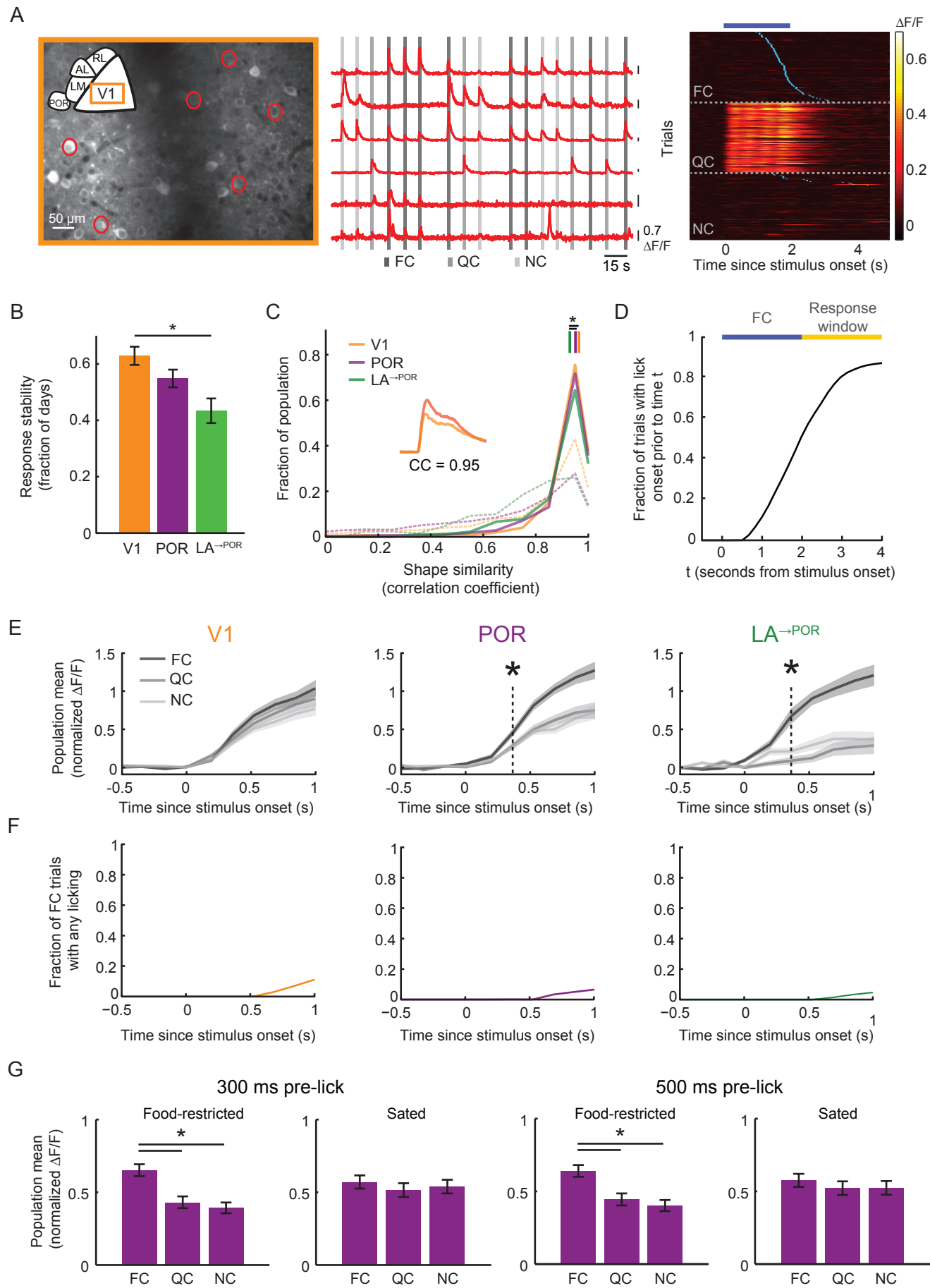


**Figure S3. Related to Figure 2. Visually responsive neurons show high response reliability across days and are not modulated by licking**

- A. An example field of view in V1 (*left*), traces (from cells outlined in red), and an example heatmap of single-trial responses for one V1 neuron, sorted by visual cue and lick latency (blue ticks). See Figure 2 legend for more details. Note the 2 Hz oscillation across single trials in the example V1 neuron, which matches the temporal frequency of the stimulus (2 Hz).
- B. We recorded from the same neurons and axons across many imaging sessions (see also Figure 2G and 4H). Neurons in V1 and POR reliably responded to their preferred cue across the majority of imaging sessions. By contrast, response reliability across days was significantly lower in  $LA^{\rightarrow POR}$  axons than in V1 neurons ( $p=0.18$ , V1 vs. POR;  $p=0.010$ , V1 vs. LA;  $p=0.29$ , POR vs. LA; Kruskal-Wallis).
- C. For neurons in each area, the shape of the mean visually-evoked response was significantly correlated across days (e.g. correlation coefficient of mean timecourse on Day 1 with mean timecourse on Day 2) when compared to a within-day shuffled distribution (dotted lines; i.e. within-day temporal correlation with other simultaneously recorded, visually-responsive neurons or axons). However, response shapes of  $LA^{\rightarrow POR}$  axons were less similar across days than those of V1 and POR neurons. Lines above distributions signify median values of each distribution.
- D. A cumulative distribution of licking onsets across all FC trials. Note the absence of licking activity in the first 500 ms after cue onset.
- E. Population mean normalized response timecourses for V1, POR, and  $LA^{\rightarrow POR}$  recordings. The FC bias emerged in POR and  $LA^{\rightarrow POR}$  ~360 ms after cue onset, well before any licking activity began (first significant timepoint is denoted with a star).
- F. Licking activity only began > 500 ms after cue onset. Note that a small subset of trials containing licking immediately prior to or within 500 ms of cue onset were removed prior to this and any other analyses. Even at 1 s after cue onset, less than 10% of trials contained any licking activity.
- G. We recalculated the mean population response in POR, but only including neural responses up to 300 ms prior to the first lick (*left*) or up to 500 ms prior to the first lick (*right*). We observed a bias in the mean population response to the FC in POR during food-restricted, but not sated states. \*  $p<0.05$  Kruskal-Wallis. Errorbars, SEM. FC: food cue; QC: quinine cue; NC: neutral cue.

Figure S4

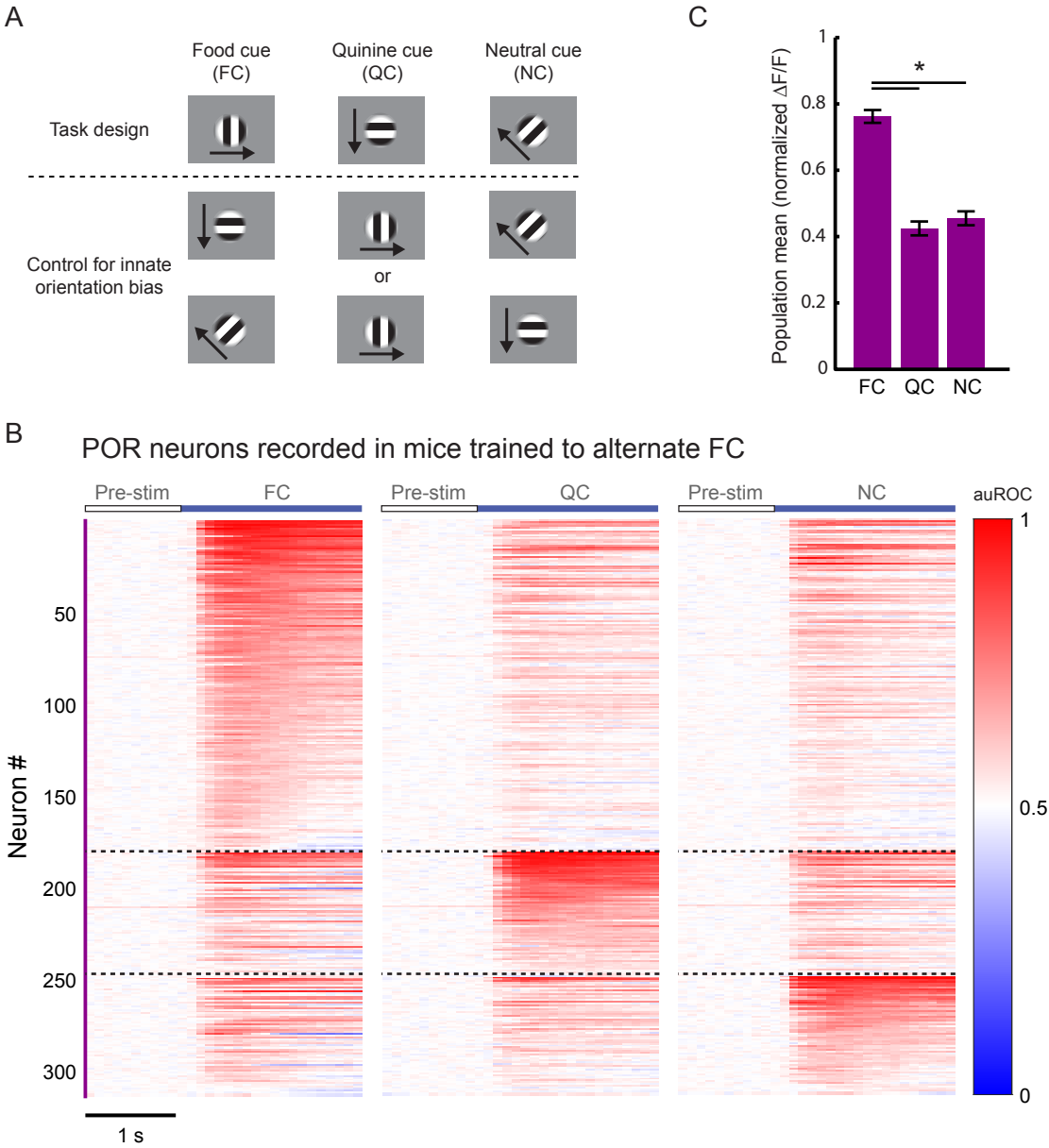


**Figure S4. Related to Figure 2. POR demonstrates a response bias to food-associated cues regardless of cue orientation**

- A. Additional mice were trained on a counterbalanced task design using the same square wave drifting gratings. We either flipped the original FC and QC (n=2 mice) or rotated the three cues with regards to trial outcome (n=1 mouse).
- B. Normalized auROC timecourses (auROC: area under the receiver operating characteristic; see Supplemental Experimental Procedures) for all significantly driven neurons (n=314) recorded in POR in these three mice. Neurons were sorted according to their preferred cue. A high proportion of POR neurons were preferentially responsive to the FC regardless of cue orientation.
- C. By normalizing cellular tuning curves to the largest response and averaging across all responsive neurons, we observed a bias in the mean population response to the FC in POR (FC vs. QC:  $p < 0.001$ , FC vs. NC:  $p < 0.001$ , QC vs. NC:  $p = 0.995$ , Kruskal-Wallis). Errorbars: SEM across cells.

Figure S5

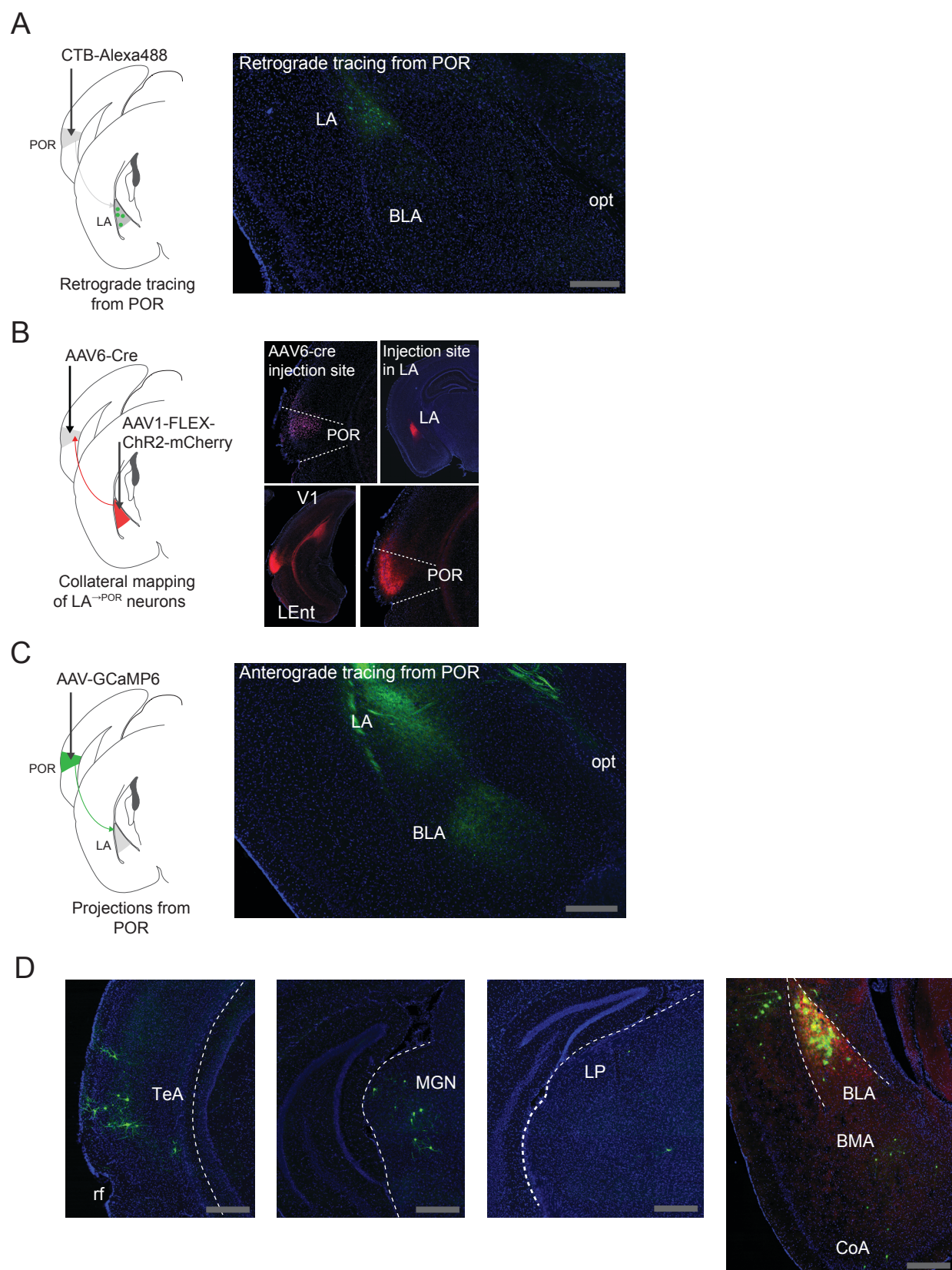


**Figure S5. Related to Figure 3. Projection-specific anterograde and retrograde tracing shows reciprocal connectivity between LA and POR**

- A. Retrograde tracing, using a 100 nL injection of fluorescently conjugated CTB, from POR demonstrates labeling of neurons in LA, with very few neurons in nearby BLA. This shows that the majority of amygdala input to POR is from LA neurons.
- B. Collateral mapping, using AAV6-cre in POR and AAV-FLEX-ChR2-mCherry in LA to label only  $LA \rightarrow POR$  neuron projections, demonstrated dense input to POR with relatively fewer projections to nearby areas in temporal cortex. AAV6-cre has pronounced retrograde transport, thus causing neurons that project to the injection site, in this case POR, to express cre-recombinase and allow for expression of cre-dependent AAVs, in this case AAV-FLEX-ChR2-mCherry, in specific afferent site.
- C. Anterograde tracing from POR demonstrates input to LA and BLA. An injection of AAV1-GCaMP6f was made into retinotopically-identified POR, determined using intrinsic signal imaging.
- D. Using projection specific rabies tracing, we identified inputs (green cells expressing rabies-GFP) to  $LA \rightarrow POR$  neurons (yellow cells containing TVA-mCherry, RG, and rabies-GFP). Briefly, TVA and rabies glycoprotein were virally expressed in the LA of vGlut2-cre mice and G-deleted rabies-GFP was injected into POR.  $LA \rightarrow POR$  neuron afferents were found in temporal association cortex (left panel), visual and auditory thalamus (middle panels) as well as in other regions of the amygdala, including basolateral and medial amygdala (right panel). These thalamic inputs, along with the previously described cortical inputs, likely provide sensory input to  $LA \rightarrow POR$  neurons. Inputs to  $LA \rightarrow POR$  neurons from BLA/BMA may provide information about value or salience to  $LA \rightarrow POR$  neurons. Red neurons: TVA-mCherry expressing cells; Green neurons: rabies-GFP expressing cells; Yellow cells: TVA and rabies-GFP expressing cells. POR: postrhinal cortex; LA: lateral amygdala; BLA: basolateral amygdala; V1: primary visual cortex; LEnt: lateral entorhinal cortex; rf: rhinal fissure; opt: optic tract; MGN: medial geniculate nucleus; TeA: temporal association cortex; LP: lateral posterior nucleus; BMA: basomedial nucleus of the amygdala; CoA: cortical amygdala; scale bar: 500  $\mu$ m.

Figure S6

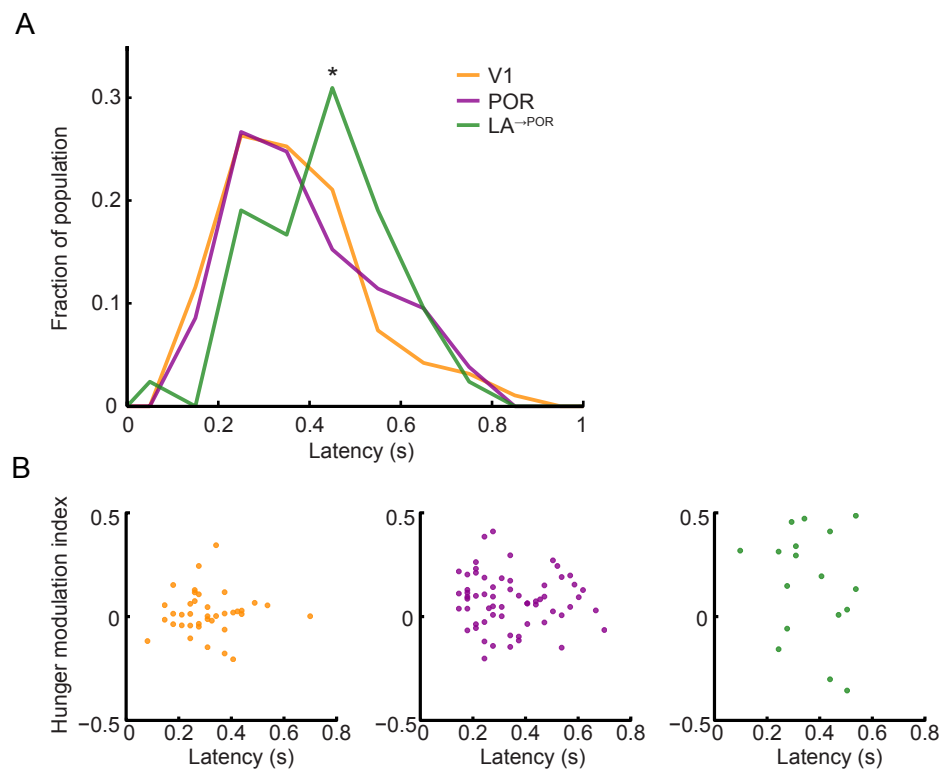


**Figure S6. Related to Figure 4. Longer cue response latencies in  $LA^{\rightarrow POR}$  than V1 or POR neurons**

- A. The distribution of neuron response latencies across areas. Response latency was defined as the first time bin exceeding two standard deviations above the mean pre-stimulus fluorescence on a trial-by-trial basis, using single-trial responses to the preferred cue for each neuron (see Supplemental Experimental Procedures). Median latency of  $LA^{\rightarrow POR}$  neurons was significantly delayed compared to V1 and POR neurons, although some  $LA^{\rightarrow POR}$  neurons had response latencies as short as ~250 ms, in agreement with previous studies (Quirk et al., 1995; Samuelson et al., 2012).
- B. Response latency was not correlated with degree of hunger modulation. \*  $p < 0.05$ , Kruskal-Wallis.



Figure S7

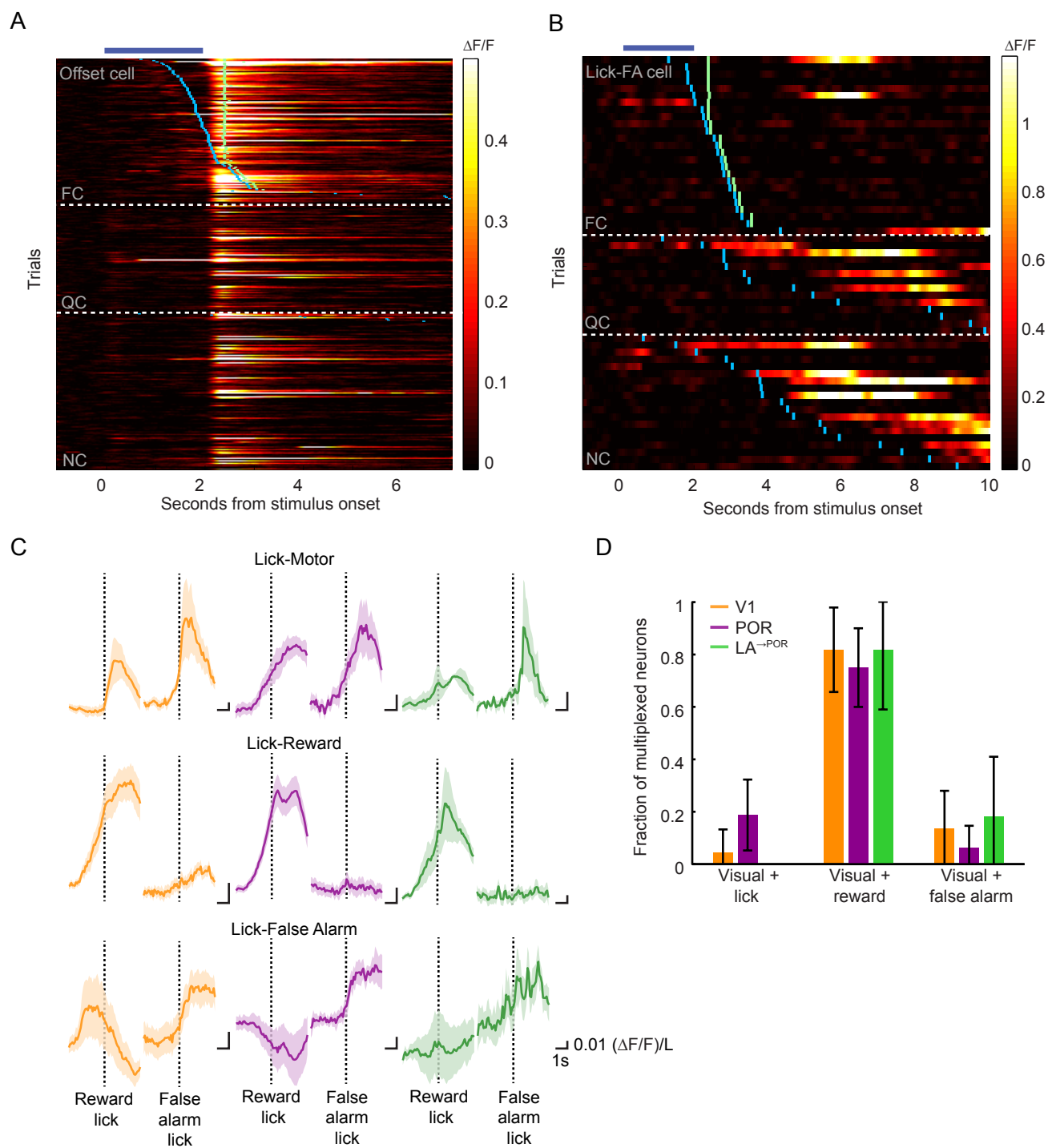


**Figure S7. Related to Figure 8. Using a general linear model to dissociate task-related responses across areas**

- A. An example of a POR neuron that responds to cue offset ('visual-offset' response). Blue tick marks denote the onset of licking on each trial, green ticks denote Ensure delivery. Note the lack of specificity in response to any particular visual cue.
- B. An example of an  $LA^{\rightarrow POR}$  axon that responds to the first lick following presentation of a QC or NC ('Lick-false alarm'). This could be interpreted as the response to the absence of an Ensure reward. Blue tick marks denote the onset of licking on each trial, while green ticks denote Ensure delivery.
- C. Average filters for all event types, from the general linear model for all neurons classified to belong to a given group in all areas (see Supplemental Experimental Procedures), aligned to lick onset (dashed line). Each dashed line corresponds to a first lick to the FC or an incorrect first lick to the QC or NC. Y-axis is in units of  $(\Delta F/F)/lick$ .
- D. Some neurons had multiplexed responses (responding both to at least one visual cue and to non-visual, task-related events such as licking; V1: 12% POR: 17%  $LA^{\rightarrow POR}$ : 12% of all task-modulated cells), though there was no significant difference across areas ( $p > 0.05$ ; Tukey's HSD multiple comparisons test among proportions). Errorbars: SEM, except in D, 95% confidence intervals. FC: food cue; QC: quinine cue; NC: neutral cue.

Figure S8

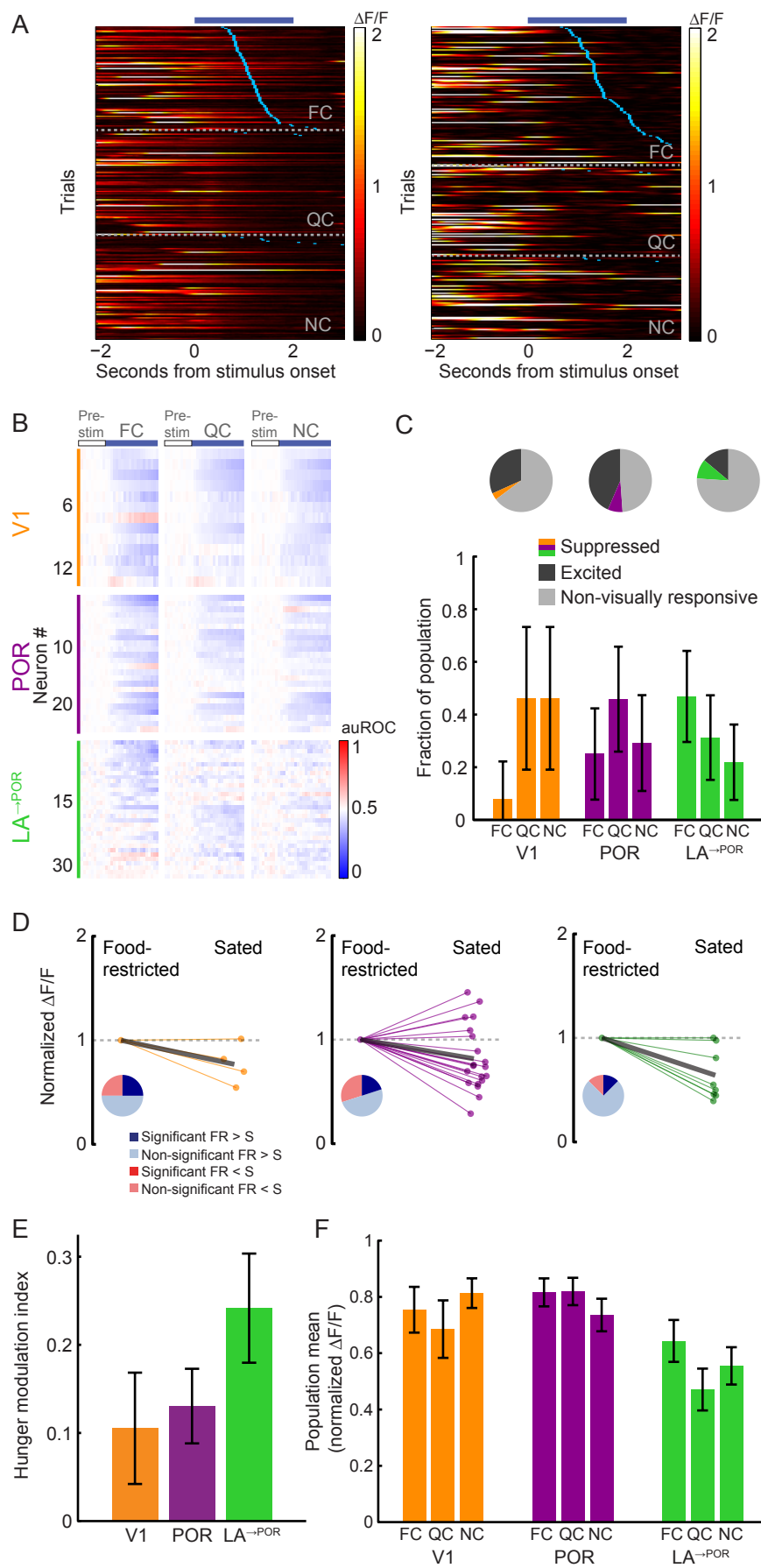


**Figure S8. Related to Figure 8. A small number of neurons in each area were strongly suppressed by visual stimuli**

- A. Examples of visually suppressed cells in POR (*left*) and LA<sup>→POR</sup> (*right*). Trials are sorted by visual cue and time to first lick. The time of the first lick on each trial is denoted in blue.
- B. Normalized (auROC) timecourses for all significantly visually suppressed neurons or axons. Each cell's response is shown for all three cues, and is sorted by preferred response. Note the lack of cue specificity in the responses of suppressed neurons in all areas.
- C. Visually suppressed cells constituted a small fraction of all recorded neurons (pie charts, visually suppressed cells in color, compared to visually excited cells labeled in dark gray; n=13 V1, n=24 POR, and n=32 LA<sup>→POR</sup> suppressed cells). Visually suppressed cells appeared mostly untuned: we did not observe a response preference to a given cue in visually suppressed cells in any area (p>0.05, Tukey's HSD multiple comparisons test among proportions).
- D. Normalized responses of all neurons in each area that were recorded in both hungry and sated states. To quantify these responses, we inverted the timecourse of all inhibited cells (timecourse \* -1) for single trials. Points that fall below 1 have smaller evoked response magnitudes when the mouse was sated (i.e. responses are less suppressed). Pie charts illustrate proportions of neurons that are increased (red), decreased (blue), significantly increased (dark red) or significantly decreased (dark blue) when sated.
- E. Comparison of the magnitude of hunger modulation across areas (p>0.05 for all comparisons; Kruskal-Wallis).
- F. There was no bias in the mean population response toward a given cue in visually suppressed cells. Errorbars, SEM, except in C, 95% confidence intervals. FC: food cue; QC: quinine cue; NC: neutral cue.

## Supplemental Experimental Procedures

### Animal preparation and surgery

All animal care and experimental procedures were approved by the Beth Israel Deaconess Medical Center Institutional Animal Care and Use Committee. Animals were housed with standard mouse chow and water provided *ad libitum*, unless specified otherwise. Mice used for *in vivo* two-photon imaging (n=15 male C57BL/6 mice, n=4 male EMX-cre mice, age at surgery: 9-15 weeks) were instrumented with a headpost and a 3 mm cranial window, centered over either primary visual cortex (window centered 2.5 mm lateral and 1 mm anterior to lambda) or lateral cortex including postrhinal cortex (window centered 4.5 mm lateral and 1 mm anterior to lambda, exact retinotopic location determined via intrinsic signal mapping; see below and Goldey et al., 2014), and allowed to recover for at least one week.

### Behavioral Training

After at least 1 week of post-surgical recovery, animals were food-restricted to 85% of their free-feeding body weight. Animals were head-fixed on a styrofoam trackball for habituation prior to any behavioral training (10 minutes to 1 hour over the course of 3-4 days). If mice displayed any signs of stress, they were immediately removed from head-fixation, and additional head-fixation sessions were added until there were no visible signs of stress (Mandelblat-Cerf et al., 2015). On the final head-fixation session, food-restricted animals were given Ensure (a high calorie liquid meal replacement) by hand via a syringe to acclimate them to the taste of Ensure. To train the animals to associate licking a lickspout with delivery of Ensure, we initially triggered delivery of Ensure (5  $\mu$ L, 0.0075 calories) to occur with every lick (with a 2.5 s inter-trial-interval with no Ensure delivery). We tracked licking behavior via an infrared beam positioned directly in front of the animal's mouth. All behavioral training was performed using MonkeyLogic (Asaad and Eskandar, 2008).

For the Go/NoGo visual discrimination task, food-restricted mice were trained to discriminate square-wave drifting gratings of different orientations. The LCD screen (Dell) used to deliver visual stimuli was positioned 20 cm from the mouse's eye. All visual stimuli were designed in Matlab (2 Hz and 0.04 cycles/degree, square wave gratings; FC: 0°, QC: 270°, NC: 135°; LA<sup>→</sup>POR imaging: fullscreen; V1 and POR imaging: 20 degree disc with sigmoidal attenuation at edges). All drifting gratings were presented for 2 s, after which the mouse had a 2 s window to respond with a lick, detected by the tongue breaking an IR beam. Stimuli were presented in pseudorandom order. Licking during the visual-cue was not punished, but also did not trigger delivery of the Ensure/quinine. Only the first lick occurring during the response window triggered delivery of Ensure/quinine. The lickspout was designed with two lick tubes (one for quinine and one for Ensure) such that the tongue contacted both tubes on each lick.

Training on the Go-NoGo task proceeded in several stages, as follows: first, once food-restricted mice reliably licked to obtain Ensure rewards during head fixation, we introduced the visual food cue (FC: 0°, 'go' trials). We initially trained animals by presenting the FC followed by unconditional delivery of the Ensure reward ('Pavlovian FC trials'; 5  $\mu$ L, 0.0075 calories). Once animals were regularly licking to the Pavlovian FC trials, we transitioned them to trials with delivery of reward conditional on the animal licking during the response window, which lasted 2 s post stimulus offset ('conditional reward'). After animals demonstrated stable licking behavior in responses to the conditional FC (lick to > 85% of FC trials), we simultaneously introduced the conditional quinine cue (QC: 270°, 'no-go' trials) and the neutral cue (NC: 135°, 'no-go' trials) for which licking resulted in the delivery of 5  $\mu$ L of 0.1 mM quinine and nothing, respectively. Initially, we biased the proportion of trials towards FC trials (FC:QC:NC, 2:1:1), but over several days we slowly increased the fraction of QC and NC trials so that all visual cues (FC, QC, NC) were presented in equal proportions prior to any recording sessions. Animals typically learned to perform the visual discrimination task in ~2-3 weeks. Even for well-trained animals, we began all imaging and behavior sessions with 2-5 Pavlovian FC trials as a "behavioral reminder." Pavlovian FC trials also occurred sporadically during imaging (0-10% of trials) to help maintain engagement. None of these Pavlovian FC

presentations were included in the data analysis. Importantly, there were no other sensory cues that mice could use to predict trial outcomes.

### **Intrinsic signal mapping of cortical areas**

To map visual cortical areas, we used epifluorescence imaging to measure changes in the intrinsic autofluorescence signal (Andermann et al., 2011) in awake mice. Autofluorescence produced by blue excitation (470 nm center, 40 nm band, Chroma) was measured through a longpass emission filter (500 nm cutoff). Images were collected using an EMCCD camera (Rolera EM-C2 QImaging, 251 x 250 pixels spanning 3 x 3 mm; 4 Hz acquisition rate) through a 4x air objective (0.28 NA, Olympus) using the Matlab Image Acquisition toolbox. For retinotopic mapping, we presented Gabor-like patches at 6-9 retinotopic locations for 8 s each (20 degree disc, 2 Hz, 0.04 cycles/degree, 45°), with an 8 s inter-stimulus interval. Analysis was performed in ImageJ and Matlab (as in Andermann et al., 2011). We isolated POR from LI/LM most easily using stimuli centered in the medial (nasal) top vs. bottom of the monitor, which translated to medial vs. lateral neuronal response locations, respectively, and we isolated POR from P using stimuli centered in the nasal vs. lateral position of the monitor, which translated to posterior vs. anterior neuronal response locations, as expected from Wang and Burkhalter, 2007. Following retinotopic mapping for identification of POR or of V1, the cranial window was removed, AAV1-Syn-GCaMP6f was injected into either V1 or POR (100-150 nL into layer 2/3; UPenn Vector Core), and the window was replaced. For lateral amygdala axon imaging, viral injection of cre-dependent AAV1-Syn-FLEX-GCaMP6f into EMX-cre mice (100-150 nL into LA/BLA; UPenn vector core) preceded lateral cortex cranial window implant by at least one week. For V1 and POR experiments, retinotopic maps and area identity were subsequently confirmed following cortical expression of GCaMP6f, using both widefield epifluorescence and two-photon calcium imaging (Figure 1E).

### **Two-photon imaging**

Two-photon imaging was performed using a resonant-scanning two-photon microscope (NeuroLabWare; 31 frames/second; 1154x512 pixels). All imaging was performed with a 16x 0.8 NA objective (Nikon) at either 1x (~800 x 400  $\mu\text{m}^2$ ), 2x (~400 x 200  $\mu\text{m}^2$ ), or 4x (~200 x 100  $\mu\text{m}^2$ ; only for LA<sup>→POR</sup> axons) digital zoom, or a 25x, 1.05 NA objective (Olympus) at 1x digital zoom (~500 x 250  $\mu\text{m}^2$ ). For axon imaging we solely used the 16x objective. All imaged fields of view (FOV) were at a depth of 115-270  $\mu\text{m}$  below the pial surface for cell body imaging and at 60-200  $\mu\text{m}$  below the pial surface for LA<sup>→POR</sup> axon imaging. Laser power measured below the objective was 25-60 mW for cell body imaging and 40-80 mW for axon imaging, using a Mai Tai DeepSee laser at 960 nm (Newport Corp.; Glickfeld et al., 2013). Imaging depth was adjusted in between runs (every 30 min) to account for slow drift in the z-plane (< 7  $\mu\text{m}$ ). To visually confirm that there were no behaviorally induced, systematic changes in z-plane, we first identified every frame (from our acquired two-photon movie) in which a stimulus appears on the screen. From these identified frame indices, we subselected only those indices for a single stimulus type (FC, QC, or NC), and assessed the mean fluorescence image for every peri-stimulus frame, from 1 second prior to stimulus onset up to 2 seconds post stimulus onset. We created a single mean image stack (averaged across trials of a given cue presentation) consisting of 93 frames for each cue (data acquired at 31 Hz). For example, the 32<sup>nd</sup> frame was the mean first frame for which that cue appeared on the screen, and the 63<sup>rd</sup> frame was the mean frame occurring one second after onset of presentation. The stability in the size of small structures in the mean fluorescence images relative to cue onset suggested a lack of systematic z-motion for any of the cues. Neurons were confirmed to be within a particular cortical area by comparison of two-photon images of surface vasculature above the imaging site with surface vasculature in widefield intrinsic autofluorescence maps, aligned to widefield retinotopic maps (see above; Andermann et al., 2011).

To assay how changes in hunger state affected behavioral and neural biases to the FC, we imaged in two blocks of trials within each imaging session, one during food-restriction and a subsequent block immediately following re-feeding. At the start of each imaging session, food-restricted mice (~85% of free-feeding weight)

performed the visual cue discrimination task. After ~400 trials (2 x 30-min imaging runs), we provided the mouse with *ad libitum* access to Ensure for 45-75 minutes using the same protocol for acclimating mice to the lick-spout (see above). During this period of time, mice consumed ~1-4 mL of Ensure and then voluntarily stopped licking for rewards (Mandelblat-Cerf et al., 2015). We then ran an additional ~400 trials (2 x 30-min imaging runs) while the mouse was “sated.” To control for changes in activity due to the passage of time rather than to changes in hunger state between the two blocks of trials (which together spanned several hours), we ran control “sham-satiation” experiments in which an equal duration of time elapsed between early and late sets of ~400 trials, but without delivery of Ensure (Figure S1A).

## Data analysis

All data analyses described below were performed with Matlab (MathWorks), Python, or ImageJ (NIH).

## Image registration and timecourse extraction

Each acquired image was first spatially downsampled by 2. To correct for motion along the imaged plane (x-y motion), each frame was registered to an average field-of-view using efficient subpixel registration methods (Bonin et al., 2011). Within each imaging session (one session/day), each run (4 runs/session) was registered to the first run of the day. Slow drifts in z-motion were typically < 7  $\mu\text{m}$  within a 30 minute run, and z-plane was adjusted between runs. Image stacks of  $\text{LA}^{\rightarrow\text{POR}}$  axons were de-noised using principal component analyses (PCA) of every pixel across time, and by user identification and removal of noise principal components (low eigenvalues; based on Mukamel et al., 2009). This resulted in axon traces with higher signal-to-noise ratios, on average, than traces from cell body imaging in POR or V1. Importantly, this difference in signal-to-noise did not underlie any of our observed effects (data not shown). Cell/axon masks and calcium activity timecourses ( $F(t)$ ) were extracted using custom implementation of common methods (Mukamel et al., 2009). To avoid use of cell masks with overlapping pixels, we only included the top 75% of pixel weights for a given mask (Ziv et al., 2013) and excluded any remaining pixels identified in multiple cell masks. Previous studies examining neural activity of long-range axons (Glickfeld et al., 2013; Makino and Komiyama, 2015; Petreanu et al., 2012) have identified individual regions-of-interest (ROIs) as single putative boutons along the axon (with each axon containing multiple highly correlated boutons). In order to not count a cell multiple times, each  $\text{LA}^{\rightarrow\text{POR}}$  ROI included signal from all boutons and the axon shaft (Mukamel et al., 2009; Nelson and Mooney, 2016). Additionally, to ensure we were not erroneously counting one  $\text{LA}^{\rightarrow\text{POR}}$  axon multiple times, we calculated the pairwise correlation coefficient of all simultaneously recorded  $\text{LA}^{\rightarrow\text{POR}}$  axon timecourses and combined the ROI masks for those with values higher than 0.7 (confirmed by eye).

Fluorescence timecourses were extracted by (non-weighted) averaging of pixels within each ROI mask. Fluorescence timecourses for neuropil within a 25  $\mu\text{m}$  sphere surrounding each ROI (but excluding adjacent ROIs and a protected ring surrounding each ROI) were also extracted ( $F_{\text{neuropil}}(t)$ : median value from the neuropil ring on each frame). Fluorescence timecourses were calculated as  $F_{\text{neuropil\_corrected}}(t) = F_{\text{ROI}}(t) - F_{\text{neuropil}}(t)$ . A running estimate of fractional change in fluorescence timecourses was calculated by subtracting a running estimate of baseline fluorescence ( $F_0(t)$ ) from  $F_{\text{neuropil\_corrected}}(t)$ , then dividing by  $F_0(t)$ :  $\Delta F/F(t) = (F_{\text{neuropil\_corrected}}(t) - F_0(t)) / F_0(t)$ .  $F_0(t)$  was estimated as the 10th (cell bodies) or 30th (axons) percentile of a trailing 32 s sliding window (Petreanu et al., 2012). All example cue-evoked timecourses shown were re-zeroed in the 1 s prior to visual stimulus onset for visualization purposes. All single-trial heatmaps were smoothed for visualization, using a sliding mean filter of 5 frames (~150 ms).

## Alignment of cell and axon masks across runs and across days

For imaging of cell bodies in POR and V1, we chose one set of cell masks for each day. For imaging of  $\text{LA}^{\rightarrow\text{POR}}$  axons, we chose individual masks for every run on each day (4 runs/day). All analyses for the alignment of cell masks across days were semi-automated with the aid of a custom Matlab GUI. To align masks across two days,

we first aligned the mean image from each day using one of three methods (depending on the degree of across day image warping): a rigid body translation, an affine image translation (which allowed for across-day image rotation), or a Delauney triangulation image transformation (for more complex image warping). The alignment used to register the mean image from each day was then applied to each individual mask. We estimated a 2D correlation coefficient to obtain an initial estimate of candidate masks of the same cell across multiple days. We then manually confirmed all suggested candidate masks across days using a custom Matlab GUI. For  $LA^{-POR}$  axons, we applied the same method but for masks across days and across runs within a day. Note that the image registration and warping techniques were applied only to masks for alignment suggestion purposes, and were never applied to cell masks for fluorescence timecourse estimation. For cell bodies, we only included those cell masks that existed across at least two imaging sessions in subsequent analyses, while for  $LA^{-POR}$  axon data we included all axon masks.

### Cell inclusion criterion

We first discarded those cells that were spontaneously active but that demonstrated very few exponential events (i.e. events were likely due to spikes or bursts of spikes, with on average  $< 5$  events/session) during an imaging session. These sparse firing cells did not show reliable peri-stimulus activity. We eliminated these cells by performing a simple ROC (receiver operating characteristic) analysis comparing pre-stimulus activity with activity following stimulus onset (0-7 s in 160 ms bins for all cues). All cells without at least one ROC value greater than 0.6 or less than 0.4 (0.5 = no change in activity from pre-stimulus baseline) were discarded.

To determine if cells were visually driven, we independently tested the cue-evoked response of each cell to each cue (FC, QC, or NC) for each day the cell was identified, using conservative criteria. For each cell and each visual cue, we calculated the mean cue-evoked response from cue onset up to 100 ms before the first lick post-stimulus onset, on every trial (to protect against behaviorally-modulated activity; no significant difference in lick latency across all 3 areas; see below and Figure 7). We binned the peri-stimulus  $\Delta F/F$  timecourse by 3 frames (~93 ms) and performed a Wilcoxon Signed-Rank test for each bin (as compared to a 1 s baseline prior to stimulus onset, with Bonferroni correction for comparison across multiple bins). We tested each bin (starting at cue onset), advancing in time until there were fewer than 10 trials contributing to a given bin (with increasing time following cue onset, there was a decreasing number of trials with data not preceded by a lick). For a cell to be considered visually responsive, we required 3 consecutive significant bins (i.e. 279 ms of significantly elevated activity from baseline). Using this criterion, we calculated the fraction of cells that was driven by each cue on each day. Cells were deemed to be visually responsive on a given day if there was a significant increase in activity to at least one visual cue. For each cell, we determined the cell's 'preferred' visual cue. If a cell was driven by only one cue, that was the preferred cue. If cells were significantly driven by more than one cue, we identified the preferred visual cue as the cue evoking the largest mean response from 0-2 s post stimulus onset (averaging activity, in each trial, up to 100 ms before first lick for trials with any licking during cue presentation).

We displayed all of the visually driven cells using an auROC (area under the receiver operating characteristic) timecourse. We calculated this timecourse each day by binning (93 ms bins) the  $\Delta F/F$  response of single trials to all 3 visual cues and comparing each bin with a baseline distribution (binned data in the 1 s prior to stimulus onset) using an ROC analysis. This analysis quantifies how discriminable these two distributions are. For example, if the two distributions are completely non-overlapping, the auROC reflects an estimate of 1 (clear increase in activity on every trial; all post-baseline firing rate values are larger than all baseline firing rate values; red in Figures 2D and 4E) or 0 (clear decrease in activity; all post-baseline firing rate values are smaller than all baseline firing rate values; blue in Figures 2D and 4E), while an auROC estimate of 0.5 indicates that the distribution of baseline and post-baseline activity is indistinguishable (white in Figures 2D and 4E; Cohen et al., 2012; Mandelblat-Cerf et al., 2015). We then averaged this auROC timecourse across all days that a cell was visually driven.

### Quantification of bias and hunger-state modulation



We quantified average population response bias towards a given cue in a given hunger state as follows. For each visually driven cell mask and for each hunger state (food-restricted, sated, sham-satiation), we calculated the mean response to all 3 visual cues from 0-1 s post stimulus onset (or up to 100 ms before first lick), and normalized this 3-point tuning curve by the largest cue response (cue-normalized  $\Delta F/F$ ). For each cell, after this normalization, any mean response to any cue that was less than zero was then set to zero (therefore, the normalized  $\Delta F/F$  responses for a given cue could range from 0-1). To calculate the bias index, we then took the response of each visually-driven cell to a given cue and divided it by the summed response to all 3 cues (bias = 1 if a cell responded to only one cue, bias = 0.33 if a cell responded equally to all 3 cues).

To quantify how changes in hunger state modulated responses to each learned cue, we calculated a hunger state-normalized  $\Delta F/F$  response. We normalized all single-trial visually-evoked responses by the mean response in the food-restricted state of each imaging session (1st two 30-minute runs of each session) from 0-1 s post-stimulus onset, for each cue that drove a significant visual response (Figure 5B-C). This allowed us to then combine trials across multiple sessions of imaging from the same cells, thus gaining statistical power in evaluating changes in response across hunger states. To determine whether single cells were significantly modulated by hunger state, we used a Wilcoxon Rank-Sum test (Figure 5C, pie charts). To quantify the effects of satiety on mean evoked responses ( $R$ ), we calculated a hunger modulation index for each cell (Figure 5D;  $(R_{FR} - R_{Sated}) / (R_{FR} + R_{Sated})$ ). To compare hunger modulation across areas, we calculated the fold change in the hunger modulation of POR and LA<sup>→POR</sup> populations as compared to V1 (Figure 5E). In addition, we made direct comparisons between V1 and POR using a 2-way ANOVA. The sample of LA<sup>→POR</sup> axons significantly driven by the QC or the NC was far smaller than for the FC, and thus QC and NC analyses were not included.

To quantify the response latency of each visually driven cell, we calculated the time post-cue onset at which the cell's response to its preferred cue first increased (for two consecutive frames) to at least two standard deviations above the pre-stimulus baseline (1 s).

We noticed that a small subset of V1 and POR neurons, and of LA<sup>→POR</sup> axons, was suppressed by the visual stimulus. To evaluate cue-induced suppression in the absence of floor effects, we only evaluated neurons with high and variable ongoing activity prior to stimulus onset that was variable across trials (Figure S8A). We quantified pre-stimulus trial-to-trial variability by calculating the pre-stimulus Fano factor (variance over mean in the 1 s prior to presentation of a visual cue). The distribution of pre-stimulus Fano factor values was well fit with an exponential distribution. Thus, to determine a threshold for sufficient pre-stimulus variability, we used a threshold of 2x the exponential distribution rate parameter determined for the V1 neuron distribution (V1 threshold = 0.37, which we also applied to all POR neurons and LA<sup>→POR</sup> axons). We then employed the identical response significance tests described above, but tested for significantly suppressed cells (see above). Therefore, suppressed cells were defined as cells with a high pre-stimulus Fano factor that additionally demonstrated significant suppression of activity during presentation of at least one type of visual cue. To quantify bias and hunger-modulation, the response traces of inhibited cells were inverted (each timecourse from each trial multiplied by -1) and the same procedures outlined above for activated cells were applied.

## Population decoding

The goal of our population analysis was to train a linear classifier to decode whether the pattern of responses of all simultaneously recorded neurons on a single FC trial occurred during the food-restricted (FR) state, or following satiation. To perform single-trial population level analyses, we used a Support Vector Machine classifier (Pagan et al., 2013) with a linear kernel. For each mouse and each session, we identified those neurons present across both FR and sated/sham-satiation states. We identified all FC trials across both states within a session, trained on even trials, and tested on odd trials (50% train / 50% test). The hyperplane was determined by taking the mean response of all neurons from 0-2 s post-FC onset. Each trial (response vector with  $n$  points for  $n$  neurons) was normalized to a unit vector in order to examine the pattern of neural responses. For all test trials, we used multiple durations of response integrated from cue onset (in steps of 200 ms) for the entire population. For each trial, we took the mean response pattern from cue onset across various durations post-stimulus onset, and predicted if that FC

presentation occurred when the animal was food-restricted or when the animal was sated (Figure 6A-C). We quantified decoder performance as the fraction of FC trials in which we correctly predicted the animal's hunger state (chance: 50%), and then compared the performance of the decoder for FR vs. sated and FR vs. sham-satiation trials at each timepoint using a Wilcoxon Rank-Sum test (with Bonferroni correction). Note that baseline, spontaneous activity differences between states could also impact classifier performance. The exact same procedure was used to decode the QC vs. the NC (Figure 6D), but in this instance we trained on a mixture of QC and NC trials, using data collected during the FR state.

### Previous trial history

To quantify the effects of trial/reward history on neural responses, we asked how the magnitude of the response to a FC (in FC-preferring cells) was affected by which visual cue was presented on the previous trial or trials. We compared the response magnitude of FC trials when the previous trial was a FC ( $R_{FC \rightarrow FC}$ ) vs. the response magnitude of FC trials when the previous trial was a non-FC ( $R_{nonFC \rightarrow FC}$ ). Since FC trials led to Ensure delivery in over 85% of trials in a typical session, trials preceded by a previous FC presentation were also typically preceded by receipt of a reward. Note that licking to a reward ceased well before the onset of the following trial (inter-trial interval, 6 s, Figure 1D), and trials with licking in the 1 s prior to cue onset and the 0.5 s after cue onset were removed from this and all other analyses. For this analysis, we grouped Pavlovian trials (rare, <10% of all FC trials) and 'conditional' FC trials (requiring operant lick response in post-stimulus response window in order to receive Ensure) when considering whether the previous trial was a FC trial or a non-FC trial. To quantify modulation by previous trial history, we created a trial history modulation index (THMI) by normalizing the difference between these two history-dependent FC responses by the mean overall FC response:  $(R_{nonFC \rightarrow FC} - R_{FC \rightarrow FC}) / R_{FC}$ . A THMI value of 0 means that the FC response is not modulated by the previous visual cue identity, a positive value means the response to a FC is greater when the previous trial was not a FC, and a negative value means the response to a FC is greater when the previous trial was a FC. Significance of individual cells was calculated by comparing that cell's THMI to a distribution of THMIs generated by shuffling individual trial indices 500 times and calculating 500 shuffled THMIs. To quantify the overall effect of trial history across areas, we estimated the absolute value of THMIs across all cells.

### Across-day analyses

For methods employed for mask alignment within and across days, as well as subsequent timecourse extraction, please see above. To quantify how stable a cell's cue-evoked response was across multiple days, we calculated what fraction of days a cell had a significant visual response to its preferred visual cue. For example, a cell that is significantly driven by the FC on 3 out of 4 days would have a stability metric of 0.75. In addition to averages of biases across single cells (Figure 2F & 4G/J) in which responses across all visually driven days were combined, we also calculated the FC bias index for each field-of-view (FOV) for each individual day, by averaging the cue-evoked response of all visually driven neurons (using the cue-normalized  $\Delta F/F$  response) in the food-restricted state (Figures 2H & 4I) and calculating the FC bias index of the FOV on that day.

The response timecourse of different neurons often differed in shape, but the shape of the response was typically quite reliable across sessions for the same neuron. To quantify this observation, we assessed the stability of the shape of a cue-evoked response (to a cell's preferred visual cue) across days (in well-trained mice) by computing a pairwise correlation coefficient of the mean response timecourse (from 1 s prior to stimulus onset to 2 s post stimulus onset) to the preferred cue for all days that a cell was significantly responsive to that cue. We compared this estimate to a null distribution, calculated as the correlation coefficient of response timecourses of pairs of cells recorded on the same day. We also quantified the trial-to-trial reliability *within* each day that a cell was driven, by calculating the Fano factor (variance over mean of the baseline-subtracted responses in the 1 s following presentation of the preferred visual cue).

## Characterization of POR in naïve, untrained mice

We performed two-photon calcium imaging in retinotopically-defined POR (see above) to characterize the response properties of POR neurons in untrained mice, as POR single-neuron visual response properties have only seldom been addressed in rodent POR neurons (Furtak et al., 2012; Vermaercke et al., 2014; Vermaercke et al., 2015; Wang and Burkhalter, 2007). We performed simple orientation mapping to generate a tuning curve for each visually responsive cell (0°, 45°, 90°, 135°, 180°, 225°, 270°, 315° drifting square wave gratings; 20° disc; 2 Hz and 0.04 cycles/degree). Note that three of these stimuli had identical direction as well as spatial and temporal frequency to the cues used in behavioral sessions (Figure 1C). To quantify the degree of orientation tuning in POR neurons, we first calculated orientation tuning curves (by averaging responses to opposite directions of motion), and then calculated an orientation selectivity index (OSI;  $(R_{\text{pref}} - R_{\text{orth}})/(R_{\text{pref}} + R_{\text{orth}})$ ;  $R_{\text{pref}}$ : response to preferred orientation;  $R_{\text{orth}}$ : response to preferred orientation + 90°; Niell and Stryker, 2008, 2010). We analyzed direction bias in this population by normalizing this 8-point tuning curve by the magnitude of the largest response, then averaging across neurons (Figure S2C).

## Anatomy and *in vitro* electrophysiology experiments

In order to characterize anatomical and functional connectivity between POR and LA, we employed several complementary approaches. To confirm glutamatergic LA axonal projections to cortex, viruses expressing Channelrhodopsin2-mCherry (AAV1-DIO-ChR2-mCherry; Penn Vector Core) or synaptophysin-mCherry (AAV8-DIO-synaptophysin-mCherry; labeling synaptic boutons only; Virovek Inc.) were injected into LA for anterograde tracing. To assess for the presence of axon collaterals of LA projections to POR or to other cortical projection targets, we injected AAV6-cre virus (AAV2/6-CAG-cre-WPRE; Penn Vector Core) into the cortical target site, allowing retrograde expression of cre-recombinase in neurons that project to the target site, and we injected cre-dependent synaptophysin-mCherry into LA (AAV8-DIO-synaptophysin-mCherry; Virovek Inc.). Four weeks after viral injection, mice were perfused and their brains were removed, cryoprotected, and sectioned on a microtome. Brain slices were then mounted on slides and imaged using a digital slide scanner (Olympus).

To determine the nature of direct LA input to POR, we performed Channelrhodopsin-assisted circuit mapping (CRACM; Petreanu et al., 2007). We injected viruses expressing Channelrhodopsin2-mCherry (AAV1-DIO-ChR2-mCherry; UPenn vector core) into the LA of 4 week old EMX-cre mice ( $n = 2$ ). Three weeks later, animals were deeply anesthetized with 7% chloral hydrate diluted in saline (500 mg/kg) and transcardially perfused with ice-cold cutting solution consisting of (in mM): 72 sucrose, 83 NaCl, 2.5 KCl, 1 NaH<sub>2</sub>PO<sub>4</sub>, 26 NaHCO<sub>3</sub>, 22 glucose, 5 MgCl<sub>2</sub>, 1 CaCl<sub>2</sub>, oxygenated with 95% O<sub>2</sub>/5% CO<sub>2</sub>, measured osmolarity: 310 – 320 mOsm/l. Mice were decapitated and brains were quickly removed into cutting solution. Then, 300- $\mu$ m-thick coronal sections including cortical area POR (see Figure S5B) were cut with a Leica VT1000S vibratome and incubated in oxygenated cutting solution at 34 °C for 45 min. Next, slices were transferred to oxygenated aCSF consisting of (in mM): 126 NaCl, 21.4 NaHCO<sub>3</sub>, 2.5 KCl, 1.2 NaH<sub>2</sub>PO<sub>4</sub>, 1.2 MgCl<sub>2</sub>, 2.4 CaCl<sub>2</sub>, 10 glucose, and stored in the same solution at room temperature (20–24°C) for at least 60 min prior to recording. A single slice was placed in the recording chamber where it was continuously superfused at a rate of 3–4 ml/min with oxygenated aCSF. POR neurons were visualized with a SliceScope microscope (Scientifica) equipped with infrared differential interference contrast.

Recordings were obtained from unidentified POR neurons in layer 2/3 using borosilicate glass microelectrodes (5–7 M $\Omega$ ) filled with a Cs<sup>+</sup>-based low Cl<sup>-</sup> internal solution containing (in mM) 135 CsMeSO<sub>3</sub>, 10 HEPES, 1 EGTA, 4 MgCl<sub>2</sub>, 4 Na<sub>2</sub>-ATP, 0.4 Na<sub>2</sub>-GTP, 10 Na<sub>2</sub>-phosphocreatine (pH 7.3 adjusted with CsOH; 295 mOsm · kg<sup>-1</sup>). Photostimulation-evoked EPSCs were recorded in whole-cell voltage-clamp mode, with membrane potential clamped and -70 mV and in presence of bicuculline (10  $\mu$ M) to block GABAAR-mediated transmission.

Recordings were made using a Multiclamp 700B amplifier, and data were filtered at 2 kHz and digitized at 10 kHz. To photostimulate ChR2+ fibers, a LED light source (473 nm; CoolLED) was used, as described previously (Kong et al., 2012). The light output was controlled by a programmable pulse stimulator, Master-8 (A.M.P.I.) and

pClamp 10.2 software (Axon Instruments). The photostimulation-evoked EPSCs detection protocol consisted of four blue light laser pulses (0.5 ms) administered 1 s apart during the first 4 s of an 8-s sweep, repeated for a total of 30 sweeps. TTX (1  $\mu$ M) and 4-AP (100  $\mu$ M) was added to the bath solution in order to identify monosynaptic connectivity.

To determine inputs to LA neurons, we employed cell type-specific rabies tracing techniques. We used a G-deleted rabies tracing approach to assess monosynaptic connectivity to LA neurons (Wickersham et al., 2007) or to LA<sup>→POR</sup> neurons. Rabies tracing was performed by virally-expressing TVA-mCherry (AAV8-FLEX-TVA-mCherry; UNC vector core) and RG (AAV8-CAG-FLEX-Rabies-G; Stanford Gene Vector and Virus Core) in cre-expressing starter cells in the LA, followed 4 weeks later by a virus expressing rabies-GFP (SADΔG-EnvA-EGFP; Salk Institute) either into the LA for retrograde tracing from all LA neurons, or into POR for projection-specific retrograde tracing (Figure 3C). It should be noted that using this technique, rabies may spread within the LA between excitatory Cre-expressing neurons that are synaptically connected to each other. Therefore some identified inputs could reflect multi-synapse inputs to LA<sup>→POR</sup> neurons. Mice were perfused 5-6 days after rabies injection, their brains removed, cryoprotected, and sectioned on a microtome. Brain slices were then mounted on slides and imaged using a digital slide scanner (Olympus).

Images of individual coronal sections were aligned with the Allen Brain Atlas to generate accurate cell locations in three-dimensional space that could be directly compared between brains. Experimenters blind to the injection location and virus type marked key locations including the cortical edge, the rhinal fissure, and the white matter tract at the medial edge of the cortex. In addition, they marked all cells infected with somatic markers (rabies-GFP) or the extent of axonal labeling and the dense core. Key locations were matched to their counterparts in the atlas of Paxinos and Watson and a warping gradient field was calculated by which all cell positions were adjusted. Finally, for the final display of the brains, we created a simulated cortical flat-mount (Figure 3D-E). Marked locations were transformed into longitudinal distances along the cortical surface from the rhinal fissure.

### General Linear Model (GLM)

We used a general linear model (GLM; Hartmann et al., 2011; Pinto and Dan, 2015) to describe non-visual, task-related activity of each cell. The  $\Delta F/F$  trace of each cell was binned at 93 ms (3 frames) and modeled as a linear combination of task-related events at varying temporal delays with respect to event onset ( $\pm 3$  sec at 93 ms intervals). The ‘event’ variables included in the GLM were: (1) the time of the first lick following FC onset, (2) the time of the first lick following any QC or NC false alarm trials, and (3) the time of stimulus offset, across all visual cues. We found that inclusion of only the lick onset explained far more variance per event than inclusion of every lick. Due to excellent behavioral performance in our task, there were few false alarm trials. Thus, we grouped false alarms to the QC and NC in order to increase trial number. We included the stimulus offset variable because we observed some cells with responses to the offset of all visual cues (Figure S7A).

We used an F-statistic to assess whether the linear output filter explained a significant amount of variance ( $p < 0.0016$  after Bonferroni correction for the number of time points tested) and we employed the following criterion to assess the sensitivity of each variable within the GLM: first, for at least one type of ‘task-modulated’ event type, the temporal filter (kernel estimate; Figure S7C) must have a significant coefficient for at least one 300 ms-long timepoint from -200 ms to 3 s post-onset of the event variable (onset of event variable is time point = 0). Second, there must be at least one significant coefficient in the 3 s after event onset that was greater than all time points in the 3 s prior to event onset. The first criterion was implemented to include cells whose filter coefficient increases immediately prior to the onset of a task-related event, and the second to ensure that visually responsive cells (Figures 2 & 4) were not incorrectly identified as ‘task-modulated’.

After running the GLM, we classified cells into 4 categories: (1) ‘Lick-motor’ cells increase their activity to lick onsets for all visual cues, (2) ‘Lick-reward’ cells increase their activity to lick onsets for the FC, (3) ‘Lick-false alarm’ cells increase their activity to lick onsets for the QC and the NC, and (4) ‘Visual offset’ cells respond to the stimulus offset for all visual cues. In Figure 8, visual offset cells were included as visually-responsive cells. We used these categories and the task-related events included in the GLM because of the highly reliable behavioral

performance in our well-trained animals (Figure 1D). Because we designed our experiments to maximize (1) accurate and consistent behavioral performance, (2) delayed reaction times to delay motor responses, as well as (3) immediate lick-triggered Ensure delivery, we could not definitively ascribe task-related responses of neurons/axons to licking *vs.* lick-induced outcomes (e.g. Ensure reward, delivery of quinine, or no outcome).

## Supplemental References

Andermann, M.L., Kerlin, A.M., Roumis, D.K., Glickfeld, L.L., and Reid, R.C. (2011). Functional specialization of mouse higher visual cortical areas. *Neuron* 72, 1025-1039.

Asaad, W.F., and Eskandar, E.N. (2008). A flexible software tool for temporally-precise behavioral control in Matlab. *J Neurosci Methods* 174, 245-258.

Bonin, V., Histed, M.H., Yurgenson, S., and Reid, R.C. (2011). Local diversity and fine-scale organization of receptive fields in mouse visual cortex. *J Neurosci* 31, 18506-18521.

Cohen, J.Y., Haesler, S., Vong, L., Lowell, B.B., and Uchida, N. (2012). Neuron-type-specific signals for reward and punishment in the ventral tegmental area. *Nature* 482, 85-88.

Furtak, S.C., Ahmed, O.J., and Burwell, R.D. (2012). Single neuron activity and theta modulation in postrhinal cortex during visual object discrimination. *Neuron* 76, 976-988.

Glickfeld, L.L., Andermann, M.L., Bonin, V., and Reid, R.C. (2013). Cortico-cortical projections in mouse visual cortex are functionally target specific. *Nat Neurosci* 16, 219-226.

Goldey, G.J., Roumis, D.K., Glickfeld, L.L., Kerlin, A.M., Reid, R.C., Bonin, V., Schafer, D.P., and Andermann, M.L. (2014). Removable cranial windows for long-term imaging in awake mice. *Nat Protoc* 9, 2515-2538.

Hartmann, T.S., Bremmer, F., Albright, T.D., and Krekelberg, B. (2011). Receptive field positions in area MT during slow eye movements. *J Neurosci* 31, 10437-10444.

Kong, D., Tong, Q., Ye, C., Koda, S., Fuller, P.M., Krashes, M.J., Vong, L., Ray, R.S., Olson, D.P., and Lowell, B.B. (2012). GABAergic RIP-Cre neurons in the arcuate nucleus selectively regulate energy expenditure. *Cell* 151, 645-657.

Makino, H., and Komiyama, T. (2015). Learning enhances the relative impact of top-down processing in the visual cortex. *Nat Neurosci* 18, 1116-1122.

Mandelblat-Cerf, Y., Ramesh, R.N., Burgess, C.R., Patella, P., Yang, Z., Lowell, B.B., and Andermann, M.L. (2015). Arcuate hypothalamic AgRP and putative POMC neurons show opposite changes in spiking across multiple timescales. *Elife* 4.

Mukamel, E.A., Nimmerjahn, A., and Schnitzer, M.J. (2009). Automated analysis of cellular signals from large-scale calcium imaging data. *Neuron* 63, 747-760.

Nelson, A., and Mooney, R. (2016). The Basal Forebrain and Motor Cortex Provide Convergent yet Distinct Movement-Related Inputs to the Auditory Cortex. *Neuron* 90, 635-648.

Niell, C.M., and Stryker, M.P. (2008). Highly selective receptive fields in mouse visual cortex. *J Neurosci* 28, 7520-7536.

Niell, C.M., and Stryker, M.P. (2010). Modulation of visual responses by behavioral state in mouse visual cortex. *Neuron* 65, 472-479.

Pagan, M., Urban, L.S., Wohl, M.P., and Rust, N.C. (2013). Signals in inferotemporal and perirhinal cortex suggest an untangling of visual target information. *Nat Neurosci* 16, 1132-1139.

Petreaanu, L., Gutnisky, D.A., Huber, D., Xu, N.L., O'Connor, D.H., Tian, L., Looger, L., and

Svoboda, K. (2012). Activity in motor-sensory projections reveals distributed coding in somatosensation. *Nature* 489, 299-303.

Petreaanu, L., Huber, D., Sobczyk, A., and Svoboda, K. (2007). Channelrhodopsin-2-assisted circuit mapping of long-range callosal projections. *Nat Neurosci* 10, 663-668.

Pinto, L., and Dan, Y. (2015). Cell-Type-Specific Activity in Prefrontal Cortex during Goal-Directed Behavior. *Neuron* 87, 437-450.

Vermaercke, B., Gerich, F.J., Ytebrouck, E., Arckens, L., Op de Beeck, H.P., and Van den Bergh, G. (2014). Functional specialization in rat occipital and temporal visual cortex. *J Neurophysiol* 112, 1963-1983.

Vermaercke, B., Van den Bergh, G., Gerich, F., and Op de Beeck, H. (2015). Neural discriminability in rat lateral extrastriate cortex and deep but not superficial primary visual cortex correlates with shape discriminability. *Front Neural Circuits* 9, 24.

Wang, Q., and Burkhalter, A. (2007). Area map of mouse visual cortex. *J Comp Neurol* 502, 339-357.

Wickersham, I.R., Finke, S., Conzelmann, K.K., and Callaway, E.M. (2007). Retrograde neuronal tracing with a deletion-mutant rabies virus. *Nat Methods* 4, 47-49.

Ziv, Y., Burns, L.D., Cocker, E.D., Hamel, E.O., Ghosh, K.K., Kitch, L.J., El Gamal, A., and Schnitzer, M.J. (2013). Long-term dynamics of CA1 hippocampal place codes. *Nat Neurosci* 16, 264-266.